Journal of Alloys and Compounds 710 (2017) 452–459

Contents lists available at ScienceDirect

Journal of Alloys and Compounds

journal homepage: http://www.elsevier.com/locate/jalcom

Excellent corrosion resistance of P and Fe modified micro-arc oxidation coating on Al alloy

Shunping Ji [a, 1], Yuchang Weng [a, 1], Zhongzhen Wu [a, *], Zhengyong Ma [a], Xiubo Tian [a], Ricky K.Y. Fu [b], Hai Lin [a], Guosong Wu [c], Paul K. Chu [b], Feng Pan [a, **]

[a] School of Advanced Materials, Peking University Shenzhen Graduate School, Shenzhen 518055, China
[b] Department of Physics and Materials Science, City University of Hong Kong, Tat Chee Avenue, Kowloon, Hong Kong, China
[c] College of Mechanics and Materials, Hohai University, Nanjing, China

ARTICLE INFO

Article history:
Received 14 February 2017
Received in revised form
23 March 2017
Accepted 26 March 2017
Available online 27 March 2017

Keywords:
Aluminum alloy
Micro-arc oxidation
Phosphate
Corrosion resistance

ABSTRACT

The corrosion resistance of aluminum and its alloys requires improvement in some applications. In this work, a 20 μm thick compact alumina coating doping Fe and P is obtained on the substrate of LY12 Al alloy by combining micro-arc oxidation (MAO) and phosphating to improve the corrosion resistance. The reaction mechanism is investigated and proposed. The coating shows a relatively small surface roughness (Ra = 0.5 μm) and a high Vickers hardness (1200 HV). The corrosion resistance is evaluated by the salt spraying test and Tafel polarization and a lifetime of up to 1800 h and a passivation potential of above 10 V are observed.

1. Introduction

Aluminum and its alloys are used in the automobile, aerospace and aviation, biomedical, and military industry due to the light weight, high strength-to-weight ratio, good casting capability, and so on [1–3]. However, the intrinsic corrosion resistance of aluminum alloys in harsh environments is not satisfactory. For instance, in a salt solution containing chloride ions, the chloride ions can destroy the native oxide film (usually below 1 μm) [4,5].

To enhance the corrosion resistance of aluminum, alloying and doping (for example, Al_2CuMg–S and Al–Mg–Si–Cu), and sacrificial anodes have been proposed but only limited improvement has been observed [6–11]. Surface treatment is an effective way to increase the hardness and corrosion resistance of aluminum and its alloys. Various organic and inorganic coatings have been applied to improve the corrosion resistance of Al and Al alloys [12–16] by techniques such as physical adsorption [17], chemical conversion [18], sol–gel deposition [4], anodic oxidation [19], and micro-arc oxidation (MAO) [20,21]. Among them, micro-arc oxidation (MAO) also referred to as plasma electrolytic oxidation (PEO), micro-plasma oxidation, or micro-arc discharge oxidation, has attracted considerable interest in recent years due to its high efficiency and low pollution cutting-edge technology for valve metals such as Al, Ti, Mg, Nb, and Ta as well as their alloys [22–25]. It has also been implemented on Al and Al alloys and the corrosion resistance lifetime determined by salt spraying test has been observed to be 336 h and longer than that achieved by other methods [26] including anodic oxidation [27,28]. The corrosion resistance can be improved further by reducing the cavities in the MAO coatings [29,30]. The phosphating process is used industrially to protect steels from corrosion by forming a compact and insoluble layer of metal phosphate on the surface. Although the coating is quite compact, the small film thickness is a bottleneck (usually less than several micrometers) thereby compromising the corrosion resistance.

Herein, we combine the advantages of MAO and phosphating to form a thick, compact, and insoluble metal phosphate coating with less cavities to enhance the corrosion resistance of LY12 aluminum alloy. An electrolyte composed by sodium hexametaphosphate and ammonium iron(III) oxalate hydrate is used to introduce Fe and P into the MAO coating and the coating delivers excellent corrosion resistance performance such as a long corrosion lifetime of 1800 h (75 days).

* Corresponding author.
** Corresponding author.
E-mail addresses: wuzz@pkusz.edu.cn (Z. Wu), Panfeng@pkusz.edu.cn (F. Pan).
[1] The authors made equal contributions.

http://dx.doi.org/10.1016/j.jallcom.2017.03.303
0925-8388/

2. Experimental details

The LY12 aluminum alloy (3.8–4.9% Cu, 1.2–1.8% Mg, 0.5% Fe, 0.5% Ni, 0–0.9% Mn, 0.25% Zn, 0.1% Cr, 0.15% Ti, 0.5% Si, and Al balance) was used as the substrate in the MAO process. The samples with dimensions of 50 mm × 25 mm × 2 mm were polished successively with SiC abrasive paper up to 2000 grit, degreased with acetone, rinsed with distilled water, and dried in a cool air prior to MAO. The electrolyte was prepared by dissolving 20 g/L of sodium hexametaphosphate ($(NaPO_3)_6$), 5 g/L of ethylenediamine tetra-acetic acid disodium salt (Na_2EDTA), and 0–8 g/L of ammonium iron(III) oxalate hydrate ($C_6H_{12}FeN_3O_{12}\cdot 3H_2O$) in distilled water. The electrolyte was placed in a stainless steel tank and the wall served as the cathode in MAO. MAO was performed at a constant

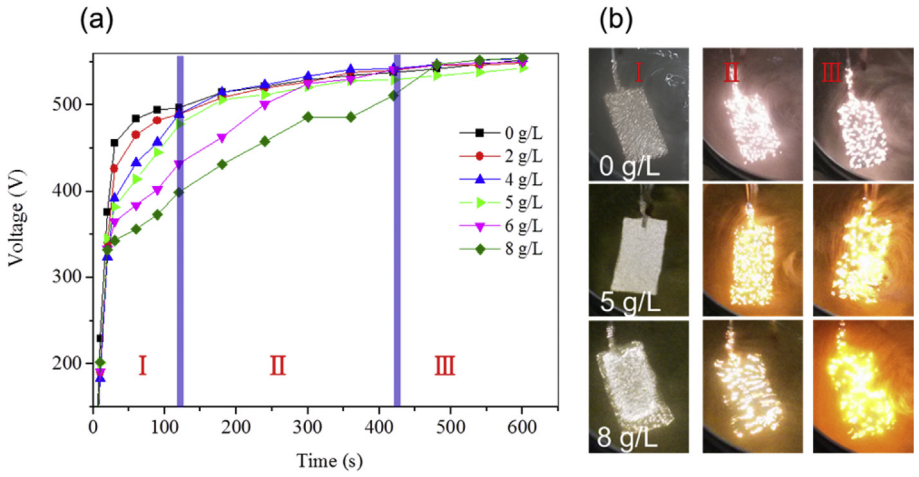

Fig. 1. (a) Voltage-Time curves for different ammonium iron(III) oxalate hydrate concentrations and (b) MAO micro-discharge images in different stages obtained at ammonium iron(III) oxalate hydrate concentrations of 0, 5, and 8 g/L.

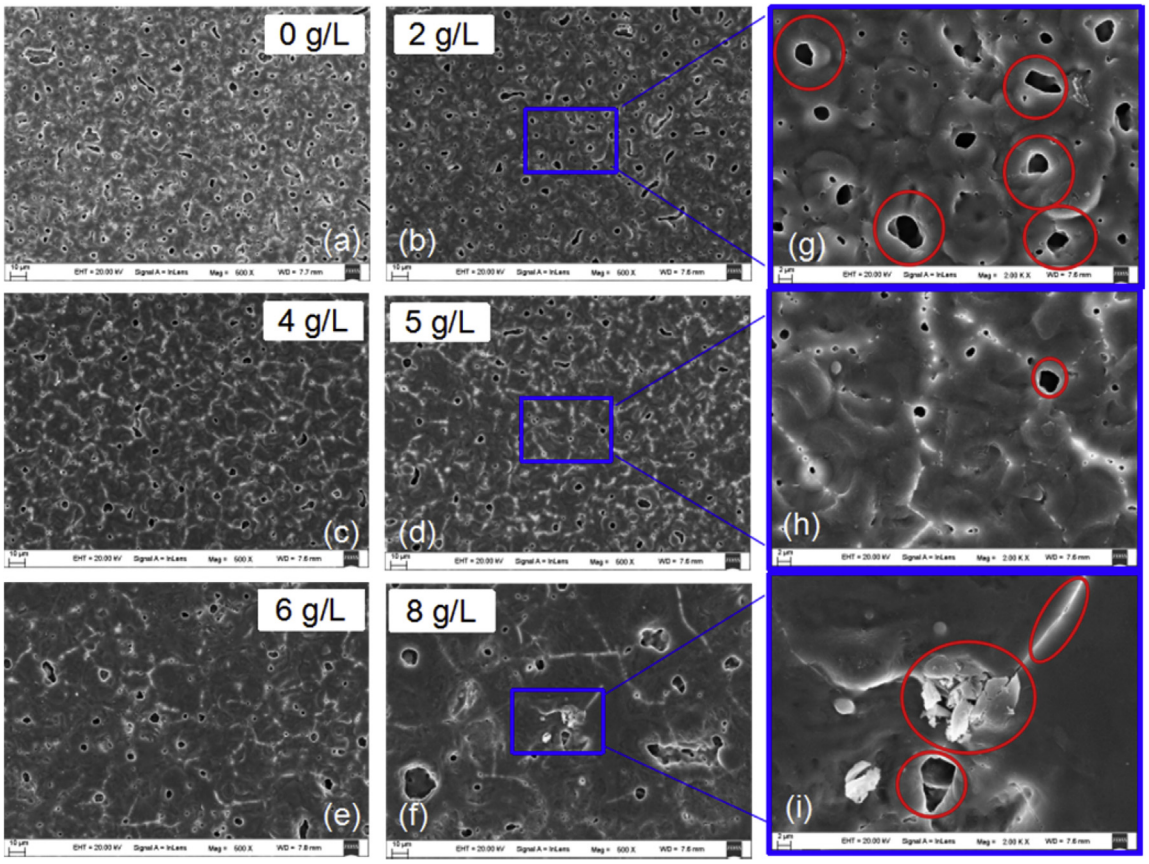

Fig. 2. SEM morphology for at different ammonium iron(III) oxalate hydrate concentrations: (a) 0 g/L, (b) 2 g/L, (c) 4 g/L, (d) 5 g/L, (e) 6 g/L, and (f) 8 g/L and (g), (h), (i) are the magnified pictures of (b), (d), (f), respectively, marked by the blue rectangles. (For interpretation of the references to colour in this figure legend, the reader is referred to the web version of this article.)

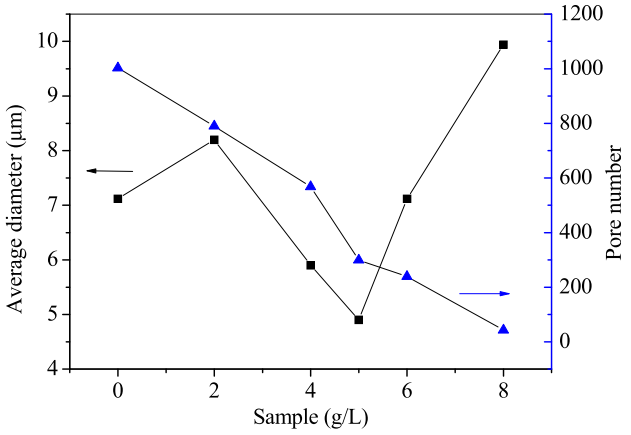

Fig. 3. Average diameter and number of pores on the surface of all the MAO coatings measured from the SEM.

current density (6 A dm^{-2}) at 200 Hz for 10 min with a duty cycle of 30% using a 20 kW AC power supply. The temperature of the electrolyte was controlled to be less than 50 °C by an external water cooling system. After MAO, the samples were washed with distilled water and then dried in air.

A field-emission scanning electron microscopy (FESEM, Carl Zeiss, SUPRA® 55) was employed to characterize the surface morphology of the samples and the elemental distribution and composition were determined by energy-dispersive X-ray spectroscopy (EDS). The phase composition was determined by powder X-ray diffraction (XRD, Bruker, D8 Advance) with a Cu target ($\lambda = 0.15418$ nm) and the data were collected at $2\theta = 10°–80°$ at a 0.01 step size. X-ray photoelectron spectroscopy (XPS, Thermo Fisher, ESCALAB 250X) was utilized to analyze the compositions of the coating samples and the spectra were referenced to the C1s peak (284.6 eV). Fourier Transform Infrared spectroscopy (FT-IR, Frontier, Perkin Elmer, USA) was conducted using KBr pellets at room temperature. The surface roughness and Vickers hardness were measured on the Surface Roughness Tester (JD220, Jitai Keyi, China) and Vickers Hardness Tester (HV-1000, Shanghai Jvjing, China), respectively. The salt spraying test was conducted on a precision salt spaying tester (SN-60A, Sannuo Instrument Co., Ltd., China) using a 5% NaCl (pH = 6.5–7.0). The Tafel curves were acquired on the electrochemical workstation (1470E, Solartron Metrology, UK) with the 3.5% NaCl solution as the electrolyte. The test was performed between −1.5 and 10 V versus saturated calomel electrode (SCE) at a scanning rate of 2 mV/s at room temperature. The corrosion current density (i_{corr}) and corrosion potential (E_{corr}) were obtained by the Tafel extrapolation method.

3. Results and discussion

Six samples are subjected to MAO in electrolytes containing different concentrations of ammonium iron(III) oxalate hydrate (0, 2, 4, 5, 6, and 8 g/L) at a constant current density of 6 A dm^{-2}, 200 Hz, and a duty cycle of 30% for 10 min. Fig. 1 shows the evolution of the micro-discharges and voltage with time. Fig. 1(a) shows that the sparking voltage falls with increasing ammonium iron(III) oxalate hydrate concentration due to increased ionic conductivity by introducing more NH_4^+ ions into the weakly acidic system (pH = 4–5). The MAO process can be roughly divided into three stages according to the different micro-discharging characteristics as shown as Fig. 1(b). In stage I, the sparks are relatively dark and tiny showing a white color and the coating is formed slowly in this stage. The main period is stage II featuring medium discharge sparks. The discharge sparks become large and sparse in stage III and local breakdown may occur on the surface due to the high power density in the local regions.

The sample morphology is displayed in Fig. 2. Some cavities like craters exist in the ceramic coatings as shown in Fig. 2(a–f). The number of pores on the surface of coatings decreases monotonically with increasing ammonium iron(III) oxalate hydrate concentration, as shown in Fig. 3, however, the average diameters of the pores decreases firstly and then increases [24]. Our results reveal an optimal ammonium iron(III) oxalate hydrate

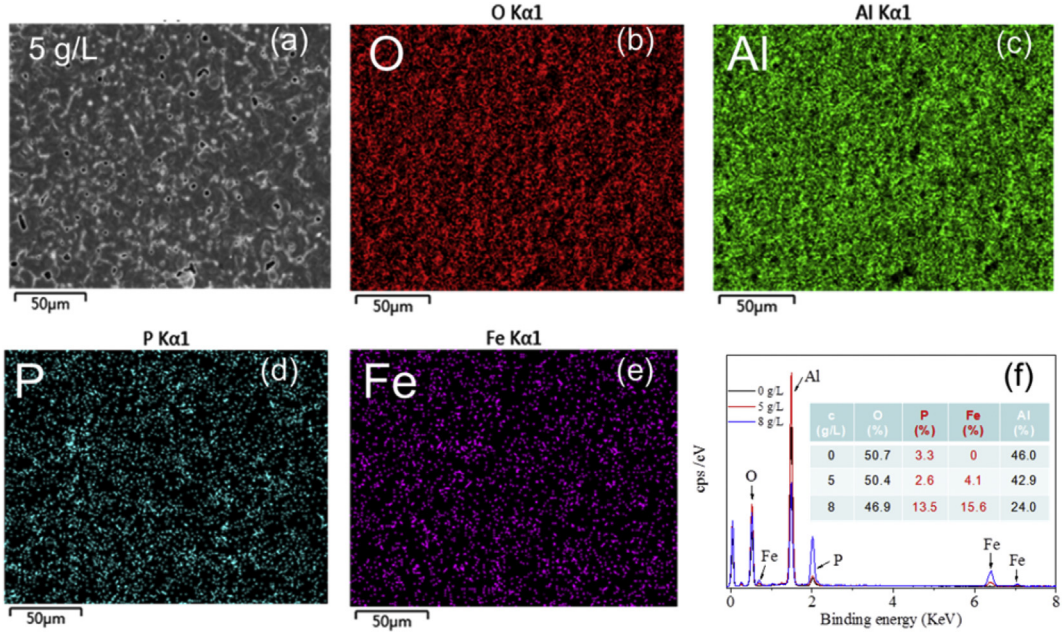

Fig. 4. EDS analysis of the sample prepared with 5 g/L concentration of ammonium iron(III) oxalate hydrate: (a) SEM morphology, (b) O, (c) Al, (d) P, (e) Fe, and (f) Elemental compositions of the 0, 5, and 8 g/L samples.

concentration of 5 g/L to obtain less and smaller cavities as shown in Fig. 2(g and h). When the concentration of ammonium iron(III) oxalate hydrate is 8 g/L [Fig. 2(f, i)], the number of cavities decreases further but the diameter of some cavities increases rapidly to about 10 μm and large cracks are observed. A possible explanation is the excessive amount of ammonium iron(III) oxalate hydrate. In stage III as shown in Fig. 1, owing to the high oxidation potential, a large amount of Fe-containing anions adsorb onto the surface of the coating resulting in extensive local oxidation. Consequently, there is not enough time to crystallize and so adhesion is compromised. In addition, defects, large cracks, and local delamination are observed and negatively impact the properties of the coating [31–33].

The SEM/EDS images are presented in Fig. 4(a–e) for the 5 g/L sample. The data confirm the introduction of P and Fe into the MAO coating and homogeneous distributions are observed. Fig. 4(f) shows the elemental concentrations on the surface of the 0, 5, and 8 g/L samples. The Fe content increases with the amount of ammonium iron(III) oxalate hydrate. It is about 4.1 wt% for the 5 g/L sample and increases to 15.6 wt% for the 8 g/L sample. However, excessive Fe in the coating weakens the mechanical properties [34,35]. The cross-sectional morphology and elemental distribution of the sample prepared with 5 g/L ammonium iron(III) oxalate hydrate are determined by 3D laser confocal microscopy and EDS as shown in Fig. 5. The coating and Al substrate can be easily distinguished and the thickness of the coating is about 20 μm. Fig. 5(b–d) show the Al, O, P, and Fe distributions in the cross-section, respectively and Fig. 5(b) shows the elemental distribution across the thickness. With increasing coating thickness, the Al concentration decreases gradually from the substrate and stabilizes in the coating, whereas the opposite trend is observed from O element. P and Fe can also be observed from the coating due to P and Fe in the electrolyte. Fe is mainly concentrated in the surface layer (about 10 μm) as shown in Fig. 5(d).

Fig. 6 shows the X-ray diffraction patterns of the MAO coatings revealing α-Al_2O_3 and γ-Al_2O_3. When the concentration of ammonium iron(III) oxalate hydrate is over 5 g/L, the diffraction peaks belong to γ-Fe_2O_3 and $AlPO_4$ can also be observed, indicating that P and Fe are incorporated as a stable phase. In particular, $AlPO_4$ is usually used in coatings as an inorganic binder to improve the

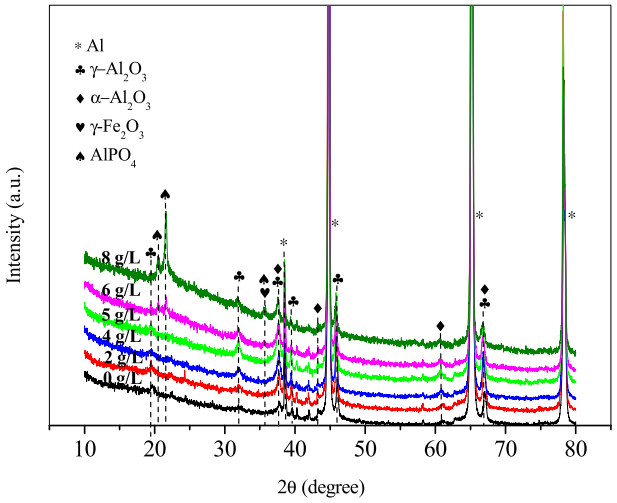

Fig. 6. XRD spectra of MAO coatings prepared with different ammonium iron(III) oxalate hydrate concentrations.

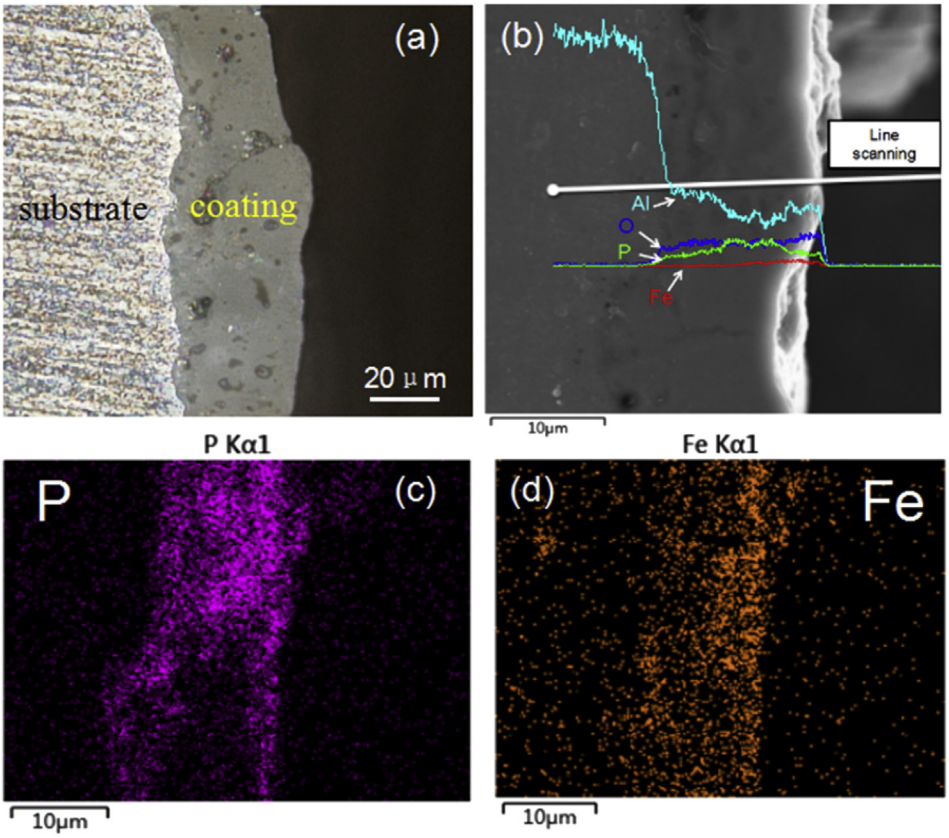

Fig. 5. (a) Cross-sectional morphology of the 5 g/L MAO coating by 3D laser confocal scanning microscopy, (b) EDS elemental line scans, (c) P, and (d) Fe.

adhesion and corrosion resistance [36–39] and Fe produces beneficial effects on the corrosion resistance and mechanical properties [40].

The XPS data in Fig. 7(a) disclose that the major components are Al, O and P. When ammonium iron(III) oxalate hydrate is added to the electrolyte, Fe appears as ferric ions and the Fe^{3+} content increases rapidly on the surface with increasing ammonium iron(III) oxalate hydrate concentration as shown in Fig. 7(b) and (d). In Fig. 7(c), the P binding energy shifts towards the low energy with increasing ammonium iron(III) oxalate hydrate concentration. P exists as $[PO_4]^{3-}$ in the coating according to XRD. Al^{3+} and Fe^{3+} are the main cations interacting with $[PO_4]^{3-}$ in the MAO process. However, the ionic radius of Fe^{3+} is larger than that of Al^{3+}, leading to a weaker interaction between Fe^{3+} and $[PO_4]^{3-}$ than that between Al^{3+} and $[PO_4]^{3-}$. Therefore, the shift in the P binding energy is attributed to the newly formed $FePO_4$, although the amount of $FePO_4$ is small. The XPS data of Al element for all six MAO coatings are also been shown in Fig. 7(e), showing that the relative intensity of Al 2p peak decreases with the increase of ammonium iron(III) oxalate hydrate concentration due to the formation of $FePO_4$.

Fourier transform infrared (FTIR) spectroscopy is employed to confirm the existence of $[PO_4]^{3-}$ in the coatings. Five samples are measured in addition to $Na_3PO_4 \cdot 10H_2O$ for comparison, as shown in Fig. 8. The IR absorption peaks of P—O stretching (ν_2, 1124 cm^{-1}), O—P—O bending (ν_3, 721 cm^{-1}), and O—P—O bending (ν_4, 488 cm^{-1}) belonging to $[PO_4]^{3-}$ can be observed indicative of the existence of $[PO_4]^{3-}$ [41]. The main absorption peaks of P—O stretching (ν_2, 1124 cm^{-1}) generate a blue shift relative to that of $Na_3PO_4 \cdot 10H_2O$ (ν_2, 1022 cm^{-1}), because that the smaller ionic radius and more charges on Al^{3+} and Fe^{3+} than Na^+ enhance the vibration frequency of P—O stretching. Except $[PO_4]^{3-}$, the peak of O—H stretching vibrational absorption (ν_1, 3500 cm^{-1}) is observed from all the

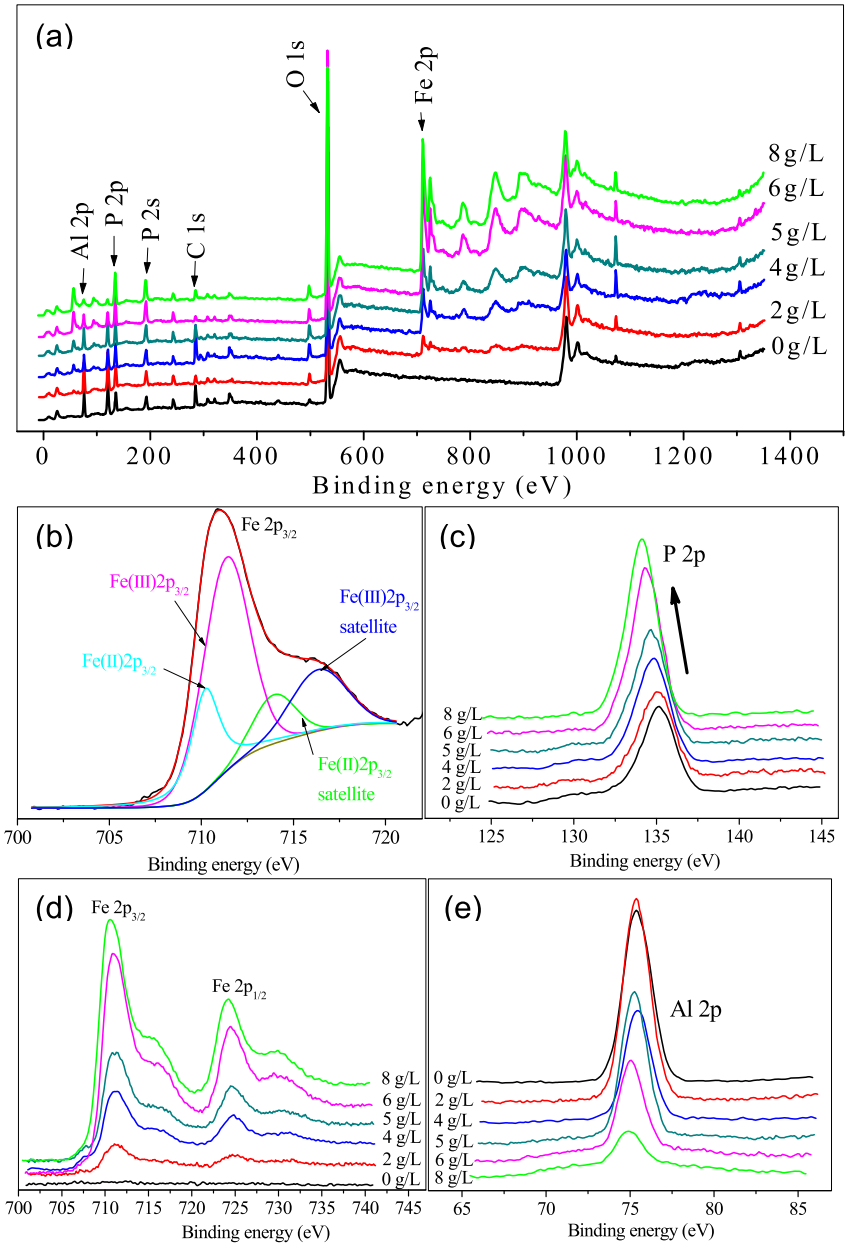

Fig. 7. XPS spectra of MAO coatings prepared with different ammonium iron(III) oxalate hydrate concentrations: (a) Survey, (b) Fe 2p for 5 g/L; (c) P 2p, (d) Fe 2p and (e) Al 2p for all coatings.

samples indicating the existence of O–H bond, however, there is no crystalline water, which has been confirmed by a TGA(Thermal Gravimetric Analyzer), suggesting a small amount of $Al_2(HPO_4)_3$ in those coatings.

According to the above characterization results, the possibly main reactions in the MAO process are proposed as follows:

$$2H_2O \rightarrow 4H^+ + O_2\uparrow + 4e \quad (1)$$

$$Al \rightarrow Al^{3+} + 3e \quad (2)$$

$$Al^{3+} + 3OH^- \rightarrow Al(OH)_3 \quad (3)$$

$$2Al(OH)_3 \rightarrow Al_2O_3 + 3H_2O \quad (4)$$

$$2Al^{3+} + 3O^{2-} \rightarrow Al_2O_3 \quad (5)$$

$$(NaPO_3)_6 + 6H_2O \rightarrow 6Na^+ + 6H_2PO_4^- \quad (6)$$

$$Al_2O_3 + 2H_2PO_4^- + 6H^+ \rightarrow 2AlPO_4 + 3H_2O \quad (7)$$

$$2Fe(C_2O_4)_3^{3-} + 3H_2O \rightarrow Fe_2O_3 + 12CO_2\uparrow + 6H^+ + 12e \quad (8)$$

$$Fe_2O_3 + 2H_2PO_4^- + 6H^+ \rightarrow 2FePO_4 + 3H_2O \quad (9)$$

Al_2O_3 is produced according to Equations (1)–(5) during the initial stage in MAO [42]. The electrolyte is heated by the arc discharge and hydrolysis of $(NaPO_3)_6$ is accelerated as shown by Equation (6) [43]. Ammonium iron(III) oxalate hydrate increases the acidity of the electrolyte and more $H_2PO_4^-$ is generated (pH: 4–5). This does not happen in alkaline electrolytes comprising silicate [44,45]. With the generation of the $H_2PO_4^-$ and increase in the discharge power with coating thickness, Al_2O_3 reacts with $H_2PO_4^-$ and $AlPO_4$ to produce the surface coatings according to Equation (7), as consistent with the XRD and FTIR results in Figs. 6 and 8. No obvious $AlPO_4$ diffraction peaks can be observed when the ammonium iron(III) oxalate hydrate concentration is less than 5 g/L because there is too little $AlPO_4$ generation. The formation of $AlPO_4$ results in reduced Al content and increased P content in the coating as revealed by the cross-sectional EDS map in Fig. 5(b). As the coating forms, the discharge power increases to more than 500 V and the anion $Fe(C_2O_4)_3^{3-}$ can be oxidized to produce ferric oxide and carbon dioxide, both of which are confirmed by XRD and Litmus paper according to Equation (8). The Fe_2O_3 stays on the surface of the coatings corresponding to the EDS line scan showing rapidly increasing Fe concentration in the outermost layer of the coating. Finally, the small amount of $FePO_4$ observed by XPS may be produced by the reaction between Fe_2O_3 and $H_2PO_4^-$ in Equation (9).

The Vickers hardness and surface roughness of the ceramic coatings prepared with different ammonium iron(III) oxalate hydrate concentrations are shown in Fig. 9. The smallest surface roughness (R_a) of about 0.5 μm is achieved at an ammonium iron(III) oxalate hydrate concentration of 4–5 g/L. The low surface roughness suggests decreased number and size of cavities consistent with the SEM micrographs. Although the amount of cavities is reduced when the concentration of ammonium iron(III) oxalate hydrate is above 5 g/L, the surface roughness increases rapidly due to the generation of larger cavities size, cracks, as well as coating delamination. The Vickers hardness of all the coated samples are larger than that of the pristine LY12 Al alloy sample which has a hardness of under 120 HV. The hardness reaches about 650 HV after MAO without ammonium iron(III) oxalate hydrate. When ammonium iron(III) oxalate hydrate is introduced into the electrolyte, the hardness increases further. The largest hardness of 1200 HV arises from the new P and Fe phases when the concentration of ammonium iron(III) oxalate hydrate is 5 g/L and it is ten times that of the pristine Al sample and nearly twice that of the MAO sample without ammonium iron(III) oxalate hydrate. However, the hardness declines gradually when the concentration of ammonium iron(III) oxalate hydrate is over 5 g/L and it may be attributed to defects arising from overly rapid growth and insufficient crystallization.

The photographs of selected samples (pristine Al, 0 g/L, 2 g/L and 5 g/L) after the salt spraying test with 5 wt% NaCl are shown in Fig. 10. Lots of corrosion pits can be observed from the pristine Al sample after 400 h and the corrosion regions become larger with time. The diameter of the expanding corrosion pits reaches hundreds of micrometers after 1800 h. After MAO, the corrosion resistance is improved and a small amount of corrosion pits appear until 800 h. However, the coating corrosion deteriorates with time. The best corrosion resistance is obtained for an ammonium iron(III) oxalate hydrate concentration of 5 g/L and no obvious corrosion pits

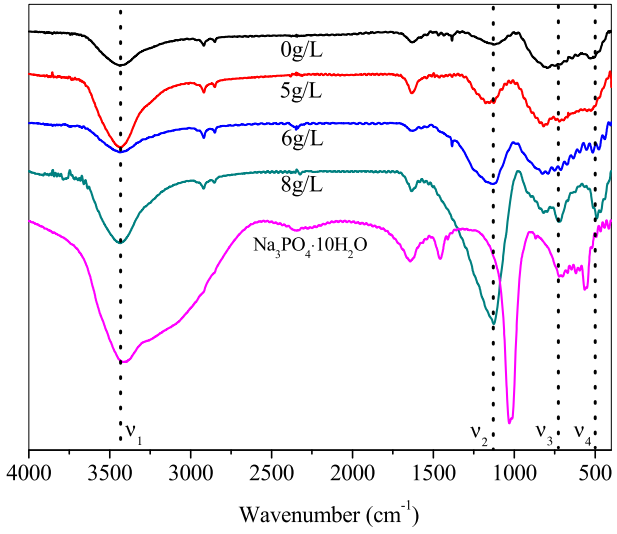

Fig. 8. FTIR spectra of MAO coatings and $Na_3PO_4 \cdot 10H_2O$.

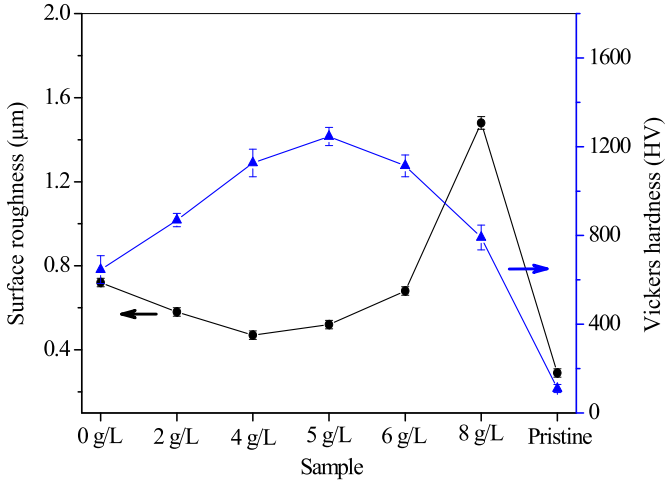

Fig. 9. Hardness and roughness of the MAO ceramic coatings prepared wtih different ammonium iron(III) oxalate hydrate concentrations.

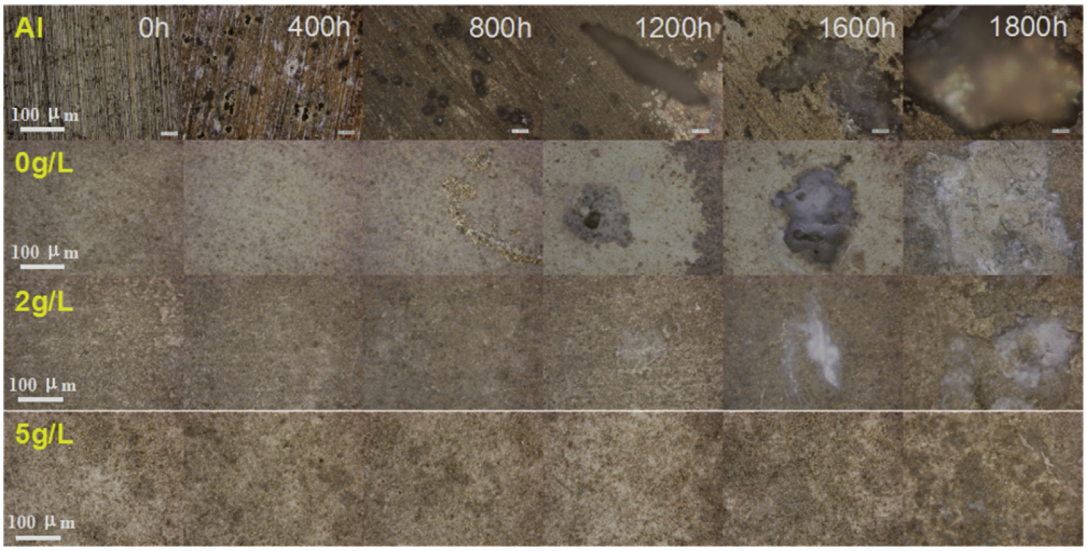

Fig. 10. Images acquired by 3D laser confocal scanning microscopy after the salt spraying for different time: Pristine Al substrate, 0 g/L, 2 g/L, and 5 g/L samples.

can be seen even after 1800 h.

Electrochemical corrosion on the uncoated and coated samples is evaluated by the Tafel curves as shown in Fig. 11. The tests are carried out after 1 h in the 3.5% NaCl solution. The largest corrosion current density (i_{corr}, 1.0×10^{-6} A cm^{-2}) reveal poor corrosion resistance on the pristine Al sample (Table 1). All the coated samples show more positive corrosion potentials (E_{corr}) than the pristine Al sample indicating better anti-corrosion performance [5,29,46,47]. The MAO sample processed without adding ammonium iron(III) oxalate hydrate shows considerable improvement in the corrosion resistance with i_{corr} being 1.1×10^{-7} A cm^{-2}. When ammonium iron(III) oxalate hydrate is added, the best corrosion resistance corresponds to an improvement of i_{corr} from 3.2 to 6.3×10^{-8} A cm^{-2}. The larger passive range of corrosion potential above 10 V with the smallest corrosion current no more than 10^{-5} A cm^{-2} can be observed when the ammonium iron(III) oxalate hydrate concentration is 5 g/L and so excellent protection can be achieved from aluminum in the chloride solution [48]. The Tafel curves are consistent with the result from the salt spraying testing with both suggesting that the dense MAO coatings with Fe and P phases and few cavities offers effective protection against corrosion for Al alloys.

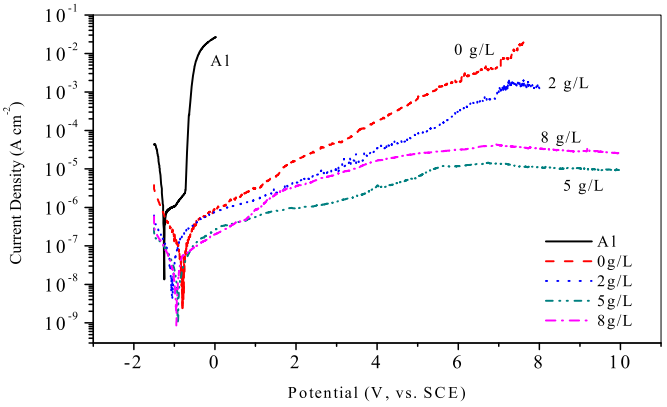

Fig. 11. Potentiodynamic polarization curves acquired in 3.5% NaCl from the pristine Al and MAO coatings prepared with different ammonium iron(III) oxalate hydrate concentrations (dE/dt = 3 mV/s).

Table 1
Electrochemical corrosion parameters measured in 3.5% NaCl from the pristine aluminum alloy and MAO coatings prepared with different ammonium iron(III) oxalate hydrate concentrations after stabilization for 1 h at the open circuit potential: corrosion current density (i_{corr}), corrosion potential (E_{corr}), and cathodic Tafel slopes (β_c).

	i_{corr} (A/cm^2)	E_{corr} (V, vs.SCE)	β_c (V/dec)
Al	1.0×10^{-6}	−1.25	0.108
0 g/L	1.1×10^{-7}	−0.8	0.537
2 g/L	6.3×10^{-8}	−1.0	0.487
5 g/L	5.0×10^{-8}	−0.91	1.058
8 g/L	3.2×10^{-8}	−0.96	0.736

4. Conclusions

A compact ceramic coating with few cavities containing stable Fe and P phases are prepared on the LY12 aluminum alloy by micro-arc oxidation (MAO) in an electrolyte composed of sodium hexametaphosphate and ammonium iron(III) oxalate hydrate. The electrochemical mechanism in the MAO discharge is proposed according to the experimental data. The optimal coating has an improved microhardness of 1200 HV and small surface roughness of 0.5 μm compared to the pristine Al substrate and MAO samples without ammonium iron(III) oxalate hydrate. The MAO coatings with the stable Fe and P phases show excellent corrosion resistance as demonstrated by the long lifetime of 1800 h in the salt spraying, enlarged passive range of corrosion potential above 10 V, as well as small corrosion currents no more than 10^{-5} A cm^{-2}.

Acknowledgements

This work was financially supported jointly by National Materials Genome Project (No. 2016YFB0700600), Natural Science Foundation of China (No. 51301004), Shenzhen Science and Technology Research Grant (JCYJ20140903102215536 and JCYJ20150828093127698), and City University of Hong Kong Applied Research Grant (ARG) No. 9667104.

References

[1] A. Heinz, A. Haszler, C. Keidel, S. Moldenhauer, R. Benedictus, W.S. Miller, Recent development in aluminium alloys for aerospace applications, Mat. Sci.

Eng. a-Struct. 280 (2000) 102–107.
[2] W.S. Miller, L. Zhuang, J. Bottema, A. Wittebrood, P. De Smet, A. Haszler, A. Vieregge, Recent development in aluminium alloys for the automotive industry, Mat. Sci. Eng. a-Struct. 280 (2000) 37–49.
[3] J. Hirsch, Recent development in aluminium for automotive applications, Trans. Nonferrous Metals Soc. China 24 (2014) 1995–2002.
[4] H. Hasannejad, T. Shahrabi, A.S. Rouhaghdam, M. Aliofkhazraei, E. Saebnoori, Investigation of heat-treatment and pre-treatment on microstructure and electrochemical properties of cerium nano-oxide films on AA7020-T6 by sol–gel methods, Appl. Surf. Sci. 254 (2008) 5683–5690.
[5] Z.-y. Wang, T. Ma, W. Han, G.-c. Yu, Corrosion behavior on aluminum alloy LY12 in simulated atmospheric corrosion process, Trans. Nonferrous Metals Soc. China 17 (2007) 326–334.
[6] T. Hashimoto, X. Zhang, X. Zhou, P. Skeldon, S.J. Haigh, G.E. Thompson, Investigation of dealloying of S phase (Al2CuMg) in AA 2024-T3 aluminium alloy using high resolution 2D and 3D electron imaging, Corros. Sci. 103 (2016) 157–164.
[7] H. Zhong, P.A. Rometsch, L. Cao, Y. Estrin, The influence of Mg/Si ratio and Cu content on the stretch formability of 6xxx aluminium alloys, Mater. Sci. Eng. A 651 (2016) 688–697.
[8] D. Battocchi, A.M. Simões, D.E. Tallman, G.P. Bierwagen, Electrochemical behaviour of a Mg-rich primer in the protection of Al alloys, Corros. Sci. 48 (2006) 1292–1306.
[9] A.M. Simões, D. Battocchi, D.E. Tallman, G.P. Bierwagen, SVET and SECM imaging of cathodic protection of aluminium by a Mg-rich coating, Corros. Sci. 49 (2007) 3838–3849.
[10] T. Jarwali, S. Nakamura, Anti-corrosion performance of bridge strands consisting of steel wires galvanised with zinc–aluminium alloy, Struct. Infrastruct. Eng. 12 (2015) 682–694.
[11] M. Guérin, J. Alexis, E. Andrieu, L. Laffont, W. Lefebvre, G. Odemer, C. Blanc, Identification of the metallurgical parameters explaining the corrosion susceptibility in a 2050 aluminium alloy, Corros. Sci. 102 (2016) 291–300.
[12] S. Gudic, L. Vrsalovic, M. Kliskic, I. Jerkovic, A. Radonic, M. Zekic, Corrosion inhibition of AA 5052 aluminium alloy in NaCl solution by different types of honey, Int. J. Electrochem S. C. 11 (2016) 998–1011.
[13] Y. Liu, P. Visser, X. Zhou, S.B. Lyon, T. Hashimoto, A. Gholinia, G.E. Thompson, G. Smyth, S.R. Gibbon, D. Graham, J.M.C. Mol, H. Terryn, An investigation of the corrosion inhibitive layers generated from lithium oxalate-containing organic coating on AA2024-T3 aluminium alloy, Surf. Interface Anal. 48 (2016) 798–803.
[14] M. Amra, K. Ranjbar, R. Dehmolaei, Mechanical properties and corrosion behavior of CeO2 and SiC incorporated Al5083 alloy surface composites, J. Mater. Eng. Perform. 24 (2015) 3169–3179.
[15] F. Zhang, C.-l. Zhang, L. Song, R.-c. Zeng, Z.-g. Liu, H.-z. Cui, Corrosion of in-situ grown MgAl-LDH coating on aluminum alloy, Trans. Nonferrous Metals Soc. China 25 (2015) 3498–3504.
[16] F. Zhang, C.-L. Zhang, L. Song, R.-C. Zeng, L.-Y. Cui, H.-Z. Cui, Corrosion resistance of superhydrophobic Mg–Al layered double hydroxide coatings on aluminum alloys, Acta Metall. Sin. Engl. Lett. 28 (2015) 1373–1381.
[17] M. Abdallah, E.M. Kamar, S. Eid, A.Y. El-Etre, Animal glue as green inhibitor for corrosion of aluminum and aluminum-silicon alloys in sodium hydroxide solutions, J. Mol. Liq. 220 (2016) 755–761.
[18] B. Valdez, S. Kiyota, M. Stoytcheva, R. Zlatev, J.M. Bastidas, Cerium-based conversion coatings to improve the corrosion resistance of aluminium alloy 6061-T6, Corros. Sci. 87 (2014) 141–149.
[19] P. Vengatesh, M.A. Kulandainathan, Hierarchically ordered self-lubricating superhydrophobic anodized aluminum surfaces with enhanced corrosion resistance, ACS Appl. Mater. interfaces 7 (2015) 1516–1526.
[20] Z. Lin, H. Yu, S. He, D. Wang, C. Chen, Effect of Na2WO4 on growth process and corrosion resistance of micro-arc oxidation coatings on 2A12 aluminum alloys in CH3COONa electrolyte, J. Mater. Eng. Perform. 25 (2015) 297–303.
[21] N. Xiang, R.G. Song, C. Wang, Q.Z. Mao, Y.J. Ge, J.H. Ding, Formation of corrosion resistant plasma electrolytic oxidation coatings on aluminium alloy with addition of sodium tungstate species, Corrosion Eng. Sci. Technol. 51 (2016) 146–154.
[22] A.L. Yerokhin, X. Nie, A. Leyland, A. Matthews, S.J. Dowey, Plasma electrolysis for surface engineering, Surf. Coat. Tech. 122 (1999) 73–93.
[23] S.P. Sah, E. Tsuji, Y. Aoki, H. Habazaki, Cathodic pulse breakdown of anodic films on aluminium in alkaline silicate electrolyte – understanding the role of cathodic half-cycle in AC plasma electrolytic oxidation, Corros. Sci. 55 (2012) 90–96.
[24] L.-Y. Cui, R.-C. Zeng, S.-K. Guan, W.-C. Qi, F. Zhang, S.-Q. Li, E.-H. Han, Degradation mechanism of micro-arc oxidation coatings on biodegradable Mg-Ca alloys: the influence of porosity, J. Alloys Compd. 695 (2017) 2464–2476.
[25] L.-Y. Cui, S.-D. Gao, P.-P. Li, R.-C. Zeng, F. Zhang, S.-Q. Li, E.-H. Han, Corrosion resistance of a self-healing micro-arc oxidation/polymethyltrimethoxysilane composite coating on magnesium alloy AZ31, Corros. Sci. 118 (2017) 84–95.
[26] I. Shchedrina, A.G. Rakoch, G. Henrion, J. Martin, Non-destructive methods to control the properties of MAO coatings on the surface of 2024 aluminium alloy, Surf. Coat. Technol. 238 (2014) 27–44.
[27] K. Dejun, W. Jinchun, Salt spray corrosion and electrochemical corrosion properties of anodic oxide film on 7475 aluminum alloy, J. Alloys Compd. 632 (2015) 286–290.
[28] S. Jegannathan, T.S.N. Sankara Narayanan, K. Ravichandran, S. Rajeswari, Evaluation of the corrosion resistance of phosphate coatings obtained by anodic electrochemical treatment, Prog. Org. Coat. 57 (2006) 392–399.
[29] T. Arunnellaiappan, N. Kishore Babu, L. Rama Krishna, N. Rameshbabu, Influence of frequency and duty cycle on microstructure of plasma electrolytic oxidized AA7075 and the correlation to its corrosion behavior, Surf. Coat. Technol. 280 (2015) 136–147.
[30] K. Du, X. Guo, Q. Guo, Y. Wang, F. Wang, Y. Tian, Effect of PEO coating microstructure on corrosion of Al 2024, J. Electrochem. Soc. 159 (2012) C597–C606.
[31] J.-H. Wang, M.-H. Du, F.-Z. Han, J. Yang, Effects of the ratio of anodic and cathodic currents on the characteristics of micro-arc oxidation ceramic coatings on Al alloys, Appl. Surf. Sci. 292 (2014) 658–664.
[32] H. Li, Y. Sun, J. Zhang, Effect of ZrO2 particle on the performance of micro-arc oxidation coatings on Ti6Al4V, Appl. Surf. Sci. 342 (2015) 183–190.
[33] T. Wei, F. Yan, J. Tian, Characterization and wear- and corrosion-resistance of microarc oxidation ceramic coatings on aluminum alloy, J. Alloys Compd. 389 (2005) 169–176.
[34] F. Jin, H. Tong, J. Li, L. Shen, P.K. Chu, Structure and microwave-absorbing properties of Fe-particle containing alumina prepared by micro-arc discharge oxidation, Surf. Coat. Technol. 201 (2006) 292–295.
[35] F. Jin, P.K. Chu, H. Tong, J. Zhao, Improvement of surface porosity and properties of alumina films by incorporation of Fe micrograins in micro-arc oxidation, Appl. Surf. Sci. 253 (2006) 863–868.
[36] E.M. Leivo, M.S. Vippola, P.P.A. Sorsa, P.M.J. Vuoristo, T.A. Mantyla, Wear and corrosion properties of plasma sprayed Al2O3 and Cr2O3 coatings sealed by aluminum phosphates, J. Therm. Spray. Technol. 6 (1997) 205–210.
[37] G. Górecki, Iron phosphate coatings—composition and corrosion resistance, Corrosion 48 (1992) 613–616.
[38] M. Vippola, S. Ahmaniemi, J. Keränen, P. Vuoristo, T. Lepistö, T. Mäntylä, E. Olsson, Aluminum phosphate sealed alumina coating: characterization of microstructure, Mater. Sci. Eng. A 323 (2002) 1–8.
[39] D. Chen, L. He, S. Shang, Study on aluminum phosphate binder and related Al2O3–SiC ceramic coating, Mater. Sci. Eng. A 348 (2003) 29–35.
[40] B.V. Jegdić, J.B. Bajat, J.P. Popić, V.B. Mišković-Stanković, Corrosion stability of polyester coatings on steel pretreated with different iron–phosphate coatings, Prog. Org. Coat. 70 (2011) 127–133.
[41] T. Dobbelaere, A.K. Roy, P. Vereecken, C. Detavernier, Atomic layer deposition of aluminum phosphate based on the plasma polymerization of trimethyl phosphate, Chem. Mater. 26 (2014) 6863–6871.
[42] H.-x. Li, R.-g. Song, Z.-g. Ji, Effects of nano-additive TiO2 on performance of micro-arc oxidation coatings formed on 6063 aluminum alloy, Trans. Nonferrous Metals Soc. China 23 (2013) 406–411.
[43] H.J. de Jager, A.M. Heyns, Study of the hydrolysis of sodium polyphosphate in water using Raman spectroscopy, Appl. Spectrosc. 52 (1998) 808–814.
[44] H. Luo, Q. Cai, B. Wei, B. Yu, D. Li, J. He, Z. Liu, Effect of (NaPO3)6 concentrations on corrosion resistance of plasma electrolytic oxidation coatings formed on AZ91D magnesium alloy, J. Alloys Compd. 464 (2008) 537–543.
[45] Q. Cai, L. Wang, B. Wei, Q. Liu, Electrochemical performance of microarc oxidation films formed on AZ91D magnesium alloy in silicate and phosphate electrolytes, Surf. Coat. Technol. 200 (2006) 3727–3733.
[46] M. Mohedano, E. Matykina, R. Arrabal, B. Mingo, A. Pardo, PEO of pre-anodized Al–Si alloys: corrosion properties and influence of sealings, Appl. Surf. Sci. 346 (2015) 57–67.
[47] W. Yang, Q. Li, Q. Xiao, J. Liang, Improvement of corrosion protective performance of organic coating on low carbon steel by PEO pretreatment, Prog. Org. Coat. 89 (2015) 260–266.
[48] P. Rodič, I. Milošev, Electrochemical and salt spray testing of hybrid coatings based on Si and Zr deposited on aluminum and its alloys, J. Electrochem. Soc. 162 (2015) C592–C600.